European Shock Tube for High Enthalpy Research

Beatriz Querido Oliveira
beatriz.querido@tecnico.ulisboa.pt
Instituto Superior Técnico, Lisboa, Portugal
July 2021

Abstract

The ESTHER shock tube is a new kinetic facility at Instituto Superior Técnico to support planetary exploration missions under the funding of the European Space Agency. The ESTHER combustion driver is operated with an initial mixture of $He/H_2/O_2$ and ignition is achieved with a laser pulse. This work main goal is to understand the influence that the ESTHER combustion driver has on the performance of the shock tube and to study the high-pressure combustion that takes place inside the driver. Besides this, a CFD high-pressure combustion study of freely expanding premixed flames of $He/H_2/O_2$ is done. It was found that the post-combustion temperature and pressure are the main driver parameters that influence the performance, where for higher pressures and temperatures, the performance is increased. By changing the driver gas diluent from He to N_2, lower performance can be achieved since with N_2 as the diluent, the gas mixture is heavier and the combustion temperature is lower. The driver performance depends mostly on the initial filling pressure and gas composition. It was found that as the dilution decreases the onset of detonations is more likely. For higher filling pressures, the amplitude of the acoustic waves increased significantly, but this behaviour would be damped if the equivalence ratio was increased. The performance and repeatability of the driver were proven. In the CFD combustion study, the main goal was to use SPARK to model 2D laminar premixed flames and obtain the laminar flame speed. Although the results do not correspond to the experimental values, some models shortfalls were identified.

Keywords: Shock tube, Combustion driver, High pressure combustion, Hydrogen, Computational Fluid Dynamics

1. Introduction

As interplanetary exploration missions become more ambitious, the engineering challenge grows, and their success strongly depends on our ability to predict and understand the multiple environments that the vehicles will be exposed to. When a spacecraft enters an atmosphere, very high speeds are achieved, and the free stream flow forms a bow shock ahead of the forebody. From previous missions, it is possible to know the performed entry speeds for different celestial bodies. In figure 1, some atmospheric entries of Mars and Titan missions, and also re-entries from sample return missions to Earth, are given.

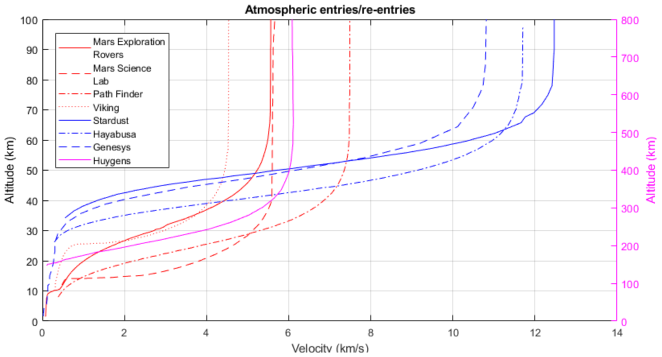

Figure 1: Entry and re-entry altitude versus speed.

Currently, the European Space Agency (ESA) is preparing exploration missions like ExoMars. To ensure the success of such missions, the use of an impulse facility such as a shock tube is very important, and, as a consequence, ESA has fostered the development of a new facility dedicated to such fundamental studies [1].

The European Shock Tube for high Enthalpy Research (ESTHER) is currently being developed at Instituto Superior Técnico under the funding of the European Space Agency. This state-of-the-art facility will be used to study high-speed flows that can exceed 10 km/s for superorbital speeds. This facility is driven by a combustion driver, and it is composed of the driver section followed by the compression tube and the shock tube, and finally a dump tank. The driver is one of the most important components of the shock tube since it will be one of the main performance boosters of the facility, and hence, its performance is by itself a challenge and the main focus of this work.

2. Shock Tube Theory

A shock tube in its most simple configuration corresponds to a tube divided into two chambers separated by a diaphragm, with a finite amount of gas. In one of the chambers, a gas at high temperature and pressure is produced, and in the second chamber, a low-pressure test gas is contained. Once the diaphragm bursts due to the high-pressure differential, a shock wave is produced and travels through the test gas, raising its temperature and pressure and accelerating it. The regions initially at high and low pressure are designated as the driver and driven sections, respectively. This working principle can be observed in figure 2, where a simple scheme of a shock tube is presented at multiple representative instants. The moving shock wave compresses and heats the test gas creating region 2, and this induces a mass movement towards the right with velocity u_2. An expansion also takes place, expanding the driver gas from region 4 to region 3. Between regions 2 and 3, a contact surface that separates the two different gases exists. This surface travels towards the right with a velocity equal to region 2. Across this slip line, the velocities and pressures are continuous, so that $p_3 = p_2$ and $u_3 = u_2$.

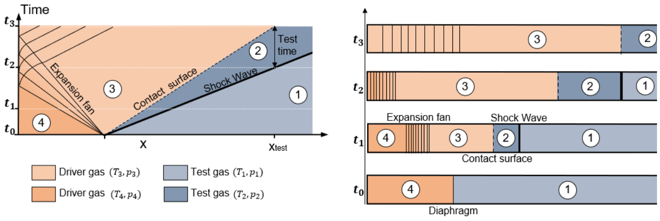

Figure 2: Shock tube scheme with x-t diagram.

2.1. Single diaphragm shock tube with uniform section

To get the performance of the simplest configuration of a shock tube, the ideal shock tube theory can be used, where it is assumed that the flow is inviscid, calorically perfect, and modelled in 1D. The velocity of the shock wave in terms of p_2/p_1 can be given by:

$$u_s = a_1 \sqrt{\frac{\gamma_1 + 1}{2\gamma_1}\left(\frac{p_2}{p_1} - 1\right) + 1}. \tag{1}$$

The shock wave pressure ratio p_2/p_1 will depend on the initial conditions of the driver and test gases. In equation 2 the relation between p_4/p_1 and p_2/p_1 is given.

$$\frac{p_4}{p_1} = \frac{p_2}{p_1}\left\{1 - \frac{(\gamma_4 - 1)\left(\frac{a_1}{a_4}\right)\left(\frac{p_2}{p_1} - 1\right)}{\sqrt{2\gamma_1\left[2\gamma_1 + (\gamma_1 + 1)\left(\frac{p_2}{p_1} - 1\right)\right]}}\right\}^{-\frac{2\gamma_4}{\gamma_4 - 1}} \tag{2}$$

For a given pressure ratio p_4/p_1, p_2/p_1 will be bigger as the sound of speed ratio a_1/a_4 is lower. Hence, if we want to increase the shock strength, hot low molecular weight gases are used in the driver and cold high molecular weight gases in the test section. The driver gas properties and composition is one of the main factors that contribute to the performance of the shock tube.

2.2. Double diaphragm shock tube with cross section area reduction

In the most simple configuration, a shock tube can not produce high velocity flows. By using a non-uniform section in the diaphragm region, unsteady expansions towards the right and left of the diaphragm will take place. With this configuration, the main advantage is related to the velocity increase that the extra forced expansion due to the area ratio can provide. For more details, see [2].

Another way to increase the performance is by adding a third section, called the compression tube. With this configuration, the facility will be composed by the driver, followed by the compression tube, and finally the shock tube that comprises the test section, with a diaphragm between every two sections (Figure 3). After the bursting of the first diaphragm, a primary shock wave is produced and travels through the intermediate gas, heating it and increasing the pressure. Once this shock wave reaches the second diaphragm, it will disintegrate, and the main shock wave is produced and travels through the test gas. With this technique, for the same pressure ratio between the driver and the shock tube, a greater shock velocity can be obtained.

By conjugating area change and the double diaphragm configuration, the performance of the facility can be increased. A detailed analysis of the performance with this configuration can be found in [3].

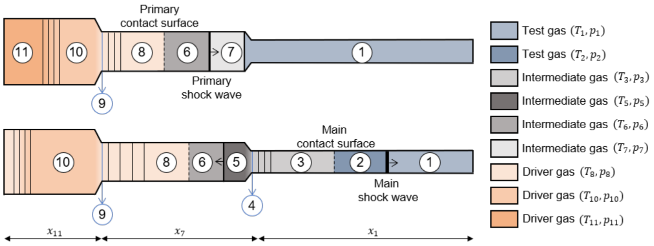

Figure 3: Shock tube with three sections with different cross section areas.

2.3. Test Time

In the previous sections, the effects of viscosity, and flow non-uniformities were neglected. In a shock tube, the test time is the difference in time between the arrival of the shock and the arrival of the contact surface at x_{test}. In an ideal shock tube, this time depends on the shock tube length, since it is assumed that the shock and contact surface move with constant velocity. But in reality, a shock layer develops between the contact surface and the shock wave. The presence of a boundary layer acts like an aerodynamic sink, removing mass in this region and causing the shock wave to de-accelerate and the contact surface to accelerate. Hence, the real test time decreases.

3. The European Shock Tube for High Enthalpy

3.1. Design

The ESTHER shock tube is composed of a driver ($L = 1.6m$, $d_1 = 200mm$), followed by the compression tube ($L = 5m$, $d_1 = 130mm$), shock tube ($L = 4m$, $d_1 = 80mm$), and lastly, the dump tank. Each of these sections has decreasing cross-section area to increase the performance. The compression tube is expected to be filled with helium between 0.01 bar and 1 bar. A dump tank will recover all the gases flowing in the wake of the shock wave.

3.2. Performance

To calculate the performance of ESTHER, the software STAGG (Shock Tube And Gas Guns) was used. The models used to predict the performance are based on the work of Alpher and White [2], Walenta [3], and Mirels [4]. For the parameter influence study, two atmospheres are used, being those the ones from Earth and Mars.

Some of the main parameters that will influence the shock tube performance will be the conditions of the driver. For higher performances, one wants the driver gas to be light, at high temperatures and pressures, and the opposite for lower performances. This can be achieved with a combustible mixture of H_2 with O_2 diluted with He or N_2 to avoid detonations.

In table 1, the theoretical results of a constant volume and adiabatic combustion process are given for two different initial gas mixtures with an initial pressure of 50 bar, each with three molar ratios between elements. These values were obtained with CEA (Chemical Equilibrium Applications) and the subscript *ad* stands for adiabatic.

Table 1: Theoretical driver gas properties for adiabatic process at constant volume and initial pressure of 50 Bar

Mixture	Molar Ratios	${p_{11}}_{ad}$ (bar)	${T_{11}}_{ad}$ (K)	${a_{11}}_{ad}$ (m/s)
He/H2/O2	9/2/1.2	470	3036	2211
	8/2/1.2	483	3140	2185
	8/2/1.3	479	3113	2142
N2/H2/O2	9/2/1.2	342	2222	940
	8/2/1.2	358	2339	965
	8/2/1.3	355	2322	960

The adiabatic equilibrium pressure is much lower for the N2 mixture, which will result in a higher initial amount of gas to reach a certain final pressure. This same behaviour occurs for the adiabatic flame temperature. These aspects, along with the fact that the heat capacity ratio is also lower for the N2 mixture, will result in significant differences in the speed of sound and hence, performance.

To simulate the performance of ESTHER, lower flame temperatures were used, since heat losses at the driver walls will occur. For the mixtures with He as the diluent, a flame temperature of 2650 K was used, and for the mixtures, with N_2 as the diluent, a temperature of 1800 K was used.

Main shock speed: In figure 4 the influence of the driver gas pressure and mixture on the mainshock speed is plotted, in (a) for the mixtures diluted with He and in (b) with N_2.

The mixtures with the highest speed of sound offer a bigger performance, with the He mixtures offering shock velocities with almost double of speed than the mixtures with N_2. With these performance differences it will be possible to recreate test flows for a wide range of velocities.

In the N_2 mixtures, the difference between the results of the main shock speed with the 8/2/1.2 and 8/2/1.3 is very slight when compared to the ones with He. This can be explained because the molar weight of oxygen is closer to the molar weight of N_2 than He that is much lighter, and hence, a bigger molar ratio of O_2 will impact the mixtures with He more. Another aspect that can be confirmed from these plots is the fact that as the driver gas pressure increases, the main shock speed also increases.

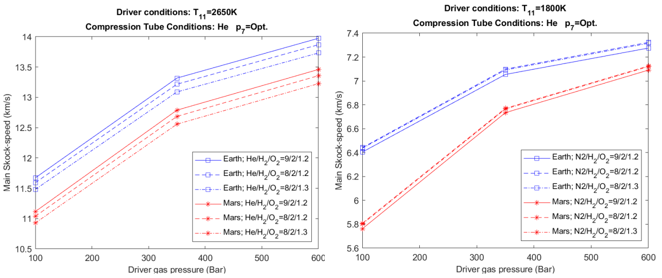

(a) (b)

Figure 4: Influence of the driver gas pressure and composition on the main shock speed for different test gases.

The influence that the final combustion temperature (T_{11}) has on the shock tube performance can also be analysed since the for the real performance of the driver, losses during the combustion process will occur, and the final temperature will depend on the combustion efficiency.

In figure 5, the influence that T_{11} has on the main shock speed is given for a He or N2 as the diluent. The temperature range used is considering a combustion efficiency from approximately 50% to 100%.

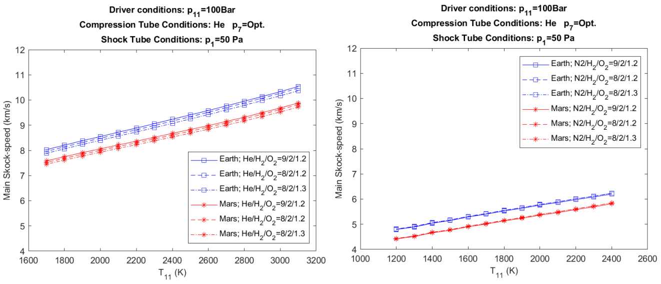

(a) (b)

Figure 5: Influence of the post combustion temperature T_{11} on the sock-tube performance with double configuration.

The post-combustion temperature has a significant influence on the shock tube performance, where for the mentioned initial conditions, it increases almost linearly with this parameter. As the temperature increases, the speed of sound of the mixture is also bigger.

With the knowledge and understanding of the combustion process that comes from the operation of the driver that will be discussed ahead, this can be another parameter used to vary the performance of the shock tube.

Test times: Using Mirels theory [4], the test times for different initial conditions, for a test section location at 4m from the second diaphragm, is given. It is assumed that the flow between the shock and contact surface is steady at each instant but also that the contact surface is moving away from the shock wave, which is not totally accurate but it gives qualitatively correct results.

The test times will be highly dependent on the main shock speed, since it is defined as the useful flow at x_{test} between the arrival of the shock and the contact surface, and this is very visible on the obtained results, that have the exact opposite behaviour as the ones in figure 4. For higher shock speeds, the test times decrease, and the opposite for lower shock speeds.

As the driver gas pressure increases, the test time decreases both for He and N2 as the diluents. When helium is used as the diluent instead of nitrogen, the test times decrease more than two times for Mars's atmosphere and more than three times for Earth's atmosphere. Considering the composition differences, the mixture with higher He dilutions has bigger test times, and the same behaviour is observed but for lower N2 dilutions.

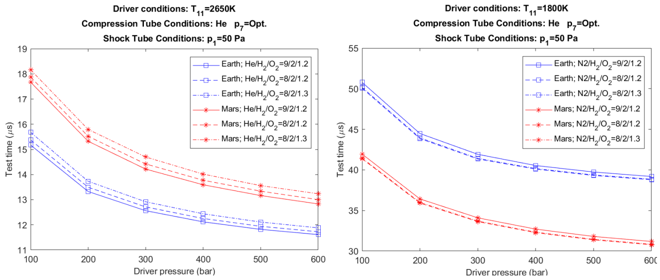

(a) (b)

Figure 6: Influence of the driver's gas pressure on the test time.

Performance Envelopes: In this section, the performance envelopes for the initial driver mixtures of $N_2/H_2/O_2$ and $He/H_2/O_2$ with a ratio of 8/2/1.3, are given. The 8/2/1.3 mixture is one of the initial filling ratios that will be used during the driver operation.

For a double configuration and a driver gas mixture of $He/H_2/O_2$, the lossless performance envelope for Earth, Mars, Titan, and the Gas Giants is given in figure 7. This envelope is limited by four boundaries, being those the performance for the upper and lower test gas pressure, and the performance when the maximum driver pressure (600 bar) and an optimal intermediate pressure is used, and on the left side, the minimum performance for $x_7 > 5m$, which is the compression tube length.

For the Earth atmosphere, the obtained performance is within some of the registered entry speeds, given in figure 1, and even with a heavier driver gas mixture, the obtained performance is suitable. For Mars and Titan's atmosphere, the registered entry speeds during missions are much lower, within 4 km/s to 7 km/s, and for this envelope, these performances are not within the boundaries.

For lower performances, the initial driver's gas mixture can be switched to $N_2/H_2/O_2$. In figure 8, the performance envelope for this mixture and the same ratio as the previous one is given. Since the lower performances are more relevant to Mars and Titan atmospheres, only these two are given. It can be seen that with these initial conditions, the registered entry speeds in figure 1 are within the performance envelopes when N_2 is used as the diluent. Furthermore, these performance envelopes do not include losses and, for real scenarios, the shock velocity will be lower.

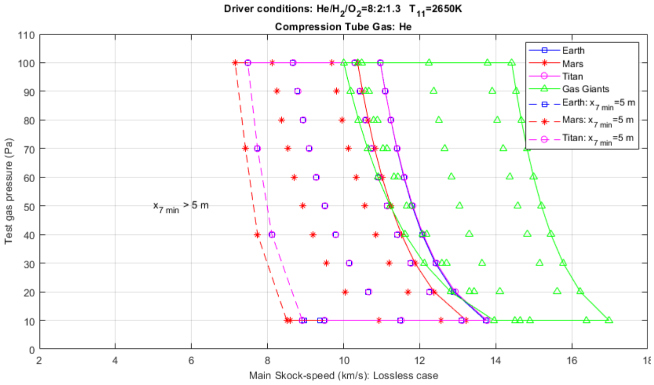

Figure 7: ESTHER performance envelope with double diaphragm configuration for a $He/H_2/O_2$ initial gas driver mixture.

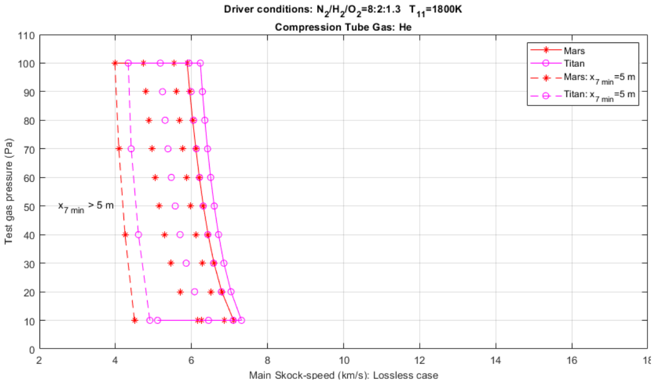

Figure 8: ESTHER performance envelope with double diaphragm configuration for a $N_2/H_2/O_2$ initial gas driver mixture.

4. Combustion Driver Operation

The performance of the driver is crucial to achieving the desired shock speeds where parameters like the pressure and gas composition of the driver, will influence the overall performance. In this section, the experimental campaign of ESTHER combustion driver is presented.

4.1. Background:Premixed flames

The combustible mixture inside the driver is at rest, and pre-mixed, and when the mixture is ignited by the laser, a flame is initiated and propagates towards the unburned mixture, forming a combustion wave. This phenomenon is categorized as premixed flame.

Concepts and definitions: In equation (3), the air-fuel equivalence ratio is given. This parameter gives a relation between the mixture ratio of the number of moles of oxidizer and fuel, divided by this same ratio for the stoichiometric molar numbers. If $\lambda > 1$ the mixture is denominated as fuel-lean, but if $\lambda < 1$, it is fuel-rich.

$$\lambda = \frac{(n_{oxi}/n_{fuel})}{(n_{oxi}/n_{fuel})_{stoi}} \quad (3)$$

In deflagrations, the chemical reaction rates have a very strong influence on the rate at which combustion occurs. For the fuel of interest in this work, H2, the overall reaction is given by:

$$2H_2 + O_2 \rightarrow 2H_2O \quad (4)$$

In a deflagration regime, the propagation of the flame in the normal direction, relative to the unburnt gases, is mentioned as the local burning velocity, S_L^0. The velocity at which the flame moves is called the flame propagation velocity S.

Regimes of flame propagation in tubes: The phenomenon behind the propagation of a flame inside closed tubes is a complex process that can be influenced by many aspects. The flame speed will depend on the regime of flame propagation, which can be classified as laminar flames, turbulent flames, both classified as deflagration, and finally, detonations. The lowest flame propagation velocity is given by the laminar regime, followed by a spectrum of turbulent flame velocities and an upper limit given by the Chapman Jouguet detonation. Represented in figure 9, the possible paths and steps of flame evolution inside a tube are given. Once the flame propagation starts, it can evolve in several ways depending on the conditions and even the source of ignition. If the ignition is weak, a laminar flame is produced, but this flame is subjected to instabilities and it can evolve to a wrinkled/cellular flame, where the surface area increases. Once the surface area increases, the mass burning rate will also increase raising the burning velocity. Because of this chain of events, turbulence can start to grow and a turbulent flame is generated. From the turbulent flame, further acceleration can take place, and the flow can transit to a detonation (Deflagration to Detonation Transition), or remain turbulent, subsonic, or supersonic.

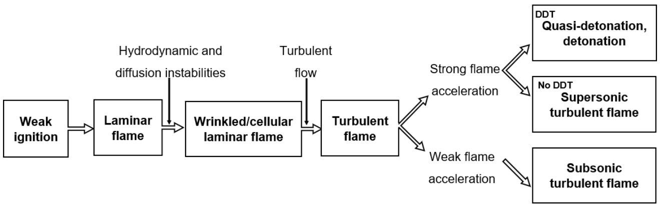

Figure 9: Sequence of flame propagation regimes inside chamber.

4.2. Experimental Set-up

In figure 10, a representation of the driver and ignition system set-up is given. On the left side of the driver, the channel where the ignition occurs for focused ignition is presented ($L = 144mm$, $d_i = 20mm$). The main combustion chamber has a cylindrical shape ($L = 1601mm$, $d_i = 200mm$). On the right, the inlet and output gas ports are represented, followed by the Kistler gauge that will record the pressure evolution along time. On the left, the ignition system is depicted. It consists of a high-power Nd:YAG laser, with a pulse wavelength of 1064 nm, 5 ns, and 200 mJ, where for focused ignition, a lens is positioned before the sapphire window to control the focal point, and for unfocused ignition it is removed.

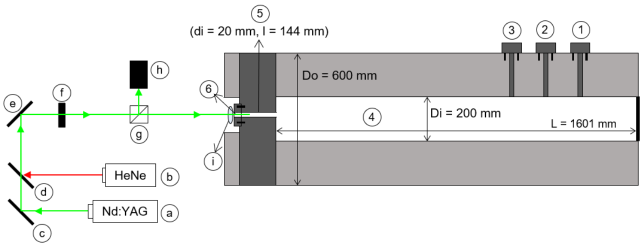

Figure 10: Ignition system and driver set-up. (1) Kistler gauge; (2) Gas output port; (3) Gas input port; (4) Combustion chamber; (5) Ignition channel; (6) Sapphire optical window; (a) High-power Nd:YAG laser 1064 nm 5 ns 200 mJ; (b) Red diode laser; (c-e) 45º mirror; (f) Half-wave plate; (g) Beam splitter cube; (h) Beam dump; (i) Bi-convex focusing lens 100 mm.

The gas filling system was designed to supply an arbitrary mixture of $He/H_2/O_2$ with a filling pressure of up to 100bar [5]. The filling is done sequentially(1st O_2, 2nd He, 3rd H_2, 4th He). The control system is automated and can be done remotely in the control bunker with the use of a Programmable Logic Controller (PLC) with an additional layer using the EPICS control system. The pressure evolution is measured with a piezoelectric pressure transducer, a Kistler gauge. The sensor is located on the third port of the combustion chamber, represented in figure 10, and is protected with a heat shield system. The signal from the sensor is further amplified with a charge amplifier and recorded in a digital storage oscilloscope.

4.3. Methodology

With the previous experimental campaign of the scaled bombe [5], it was possible to obtain some data and experience to understand some important key points and cautions when dealing with hydrogen high-pressure combustion. The first shots would be performed at lower filling pressures (10bar) and with the optimal mixture ratio to suppress instabilities obtained from the previous test campaign, being that 8:2:1.2 of $He/H_2/O_2$. If the obtained results showed that the combustion was stable, repeatability would be studied and other filling parameters would be varied. If the results showed that the combustion was not stable, the concentration of O_2 would be increased until stable combustion was achieved, since it was shown that it would suppress the acoustic instabilities. If the combustion regime was stable, the filling pressure would be increased by 10 bar.

4.4. Results

A total of 57 shots was performed. In figure 11, a representation of the initial fill parameters of the successful shots and a qualitative representation of the compression ratio is given. Each side of the triangle gives the molar fraction of He, H_2, and O_2, and the colour code the filling pressure. The circles represent shots that had a deflagration, with compression ratios smaller than the theoretical values, and the diamonds represent shots where a transition to detonation occurred and the compression ratio reached the maximum values.

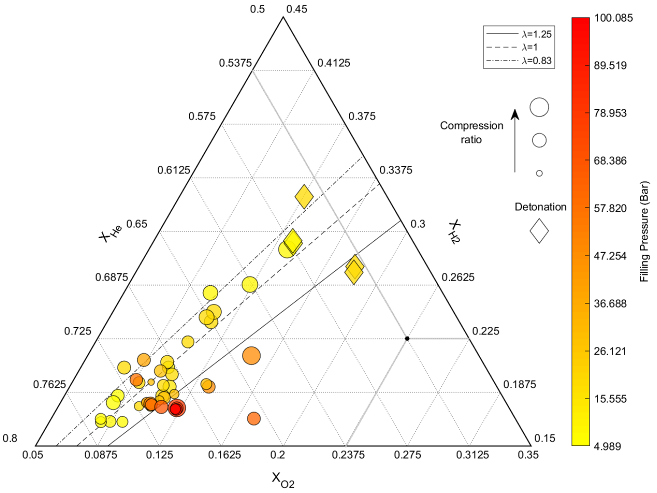

Figure 11: Initial filling parameters and qualitative compression ratio of the performed shots.

Accoustic analysis: One way to process the results and have a clearer view of the accoustic phenomena that occur inside the chamber is by using the Fast Fourier Transform on the pressure signal, a way to convert it into the frequency domain.

The natural frequencies of cylindrical chambers are given by $f = a \cdot n/(2L_{chamber}), n = 1, 2, ...$, derived by Draper in [6], where n denotes different modes or harmonics. The term related to the radial modes was ignored since for ESTHER combustion chamber the longitudinal modes will be predominant.

In figure 12, the pressure evolution of a shot with $p_{fill} = 80bar$, $\lambda = 1.39$, and $\%He = 70$, with unfocused ignition, and the respective spectrogram is given. It is possible to see two plots, one for n=1, the fundamental frequency of the chamber, and another for n=2, the first harmonic. To calculate these frequencies, the average speed of sound of the gas was calculated considering the volume ratio of burned and unburned gas and each region speed of sound. The fundamental frequency follows relatively close to the power density spectrum, where the growing wave frequency due to an increase of the speed of sound is very visible. It is only when the flame is at its final stage and closer to the pressure sensor, that the 1st harmonic is detected. On the pressure plot at $t = 0.04s$ it is possible to see the beginning of what it looks like to be a flame instability, and from there, the amplitude of the accoustic waves starts to increase. Although it is not possible to take many conclusions from this, it seems that this harmonic appeared during the beginning of the instability, or the other way around. Nevertheless, it is a clear proof that the accoustic of the chamber will influence the combustion process.

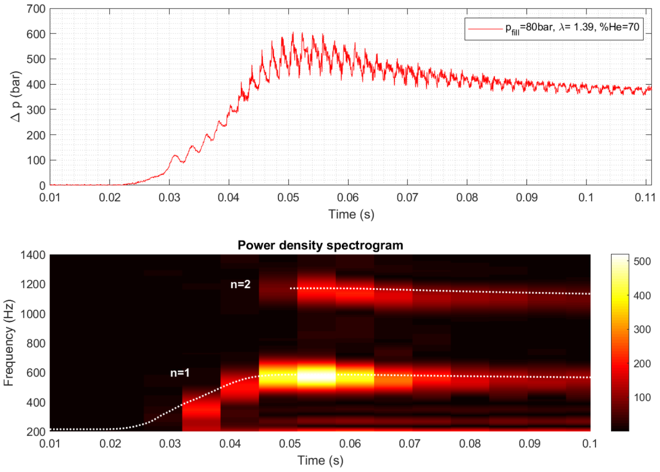

Figure 12: Short time Fourier transform of deflagration shot.

Parameter study: In this section, a comparison between the obtained results of different shots is discussed, and the observed influence of each initial parameter is analysed. These results were obtained by interpretation of the pressure profile. The compression ratio $(C.R.)$ corresponds to the division between the peak pressure and the filling pressure. For $\overline{S}$, the flame path distance divided by the combustion time was used. The average mass burning rate was calculated using the initial mass inside the chamber (m_i), divided by the combustion time. For the average acoustic wave amplitude $(\overline{p_{ac}})$, the pressure signal was filtered in order to smooth all of the accoustic waves, and this new signal was subtracted from the original one, leaving only the acoustic wave amplitude. From here, the local maximums of the absolute value of the processed signal were obtained.

Firstly, the influence of the helium percentage is given. In figure 13 two shots are compared, both with an initial filling pressure of 50 bar, and an equivalence ratio of 1.4. With a 4% difference of helium molar fraction, the obtained results are very distinct.

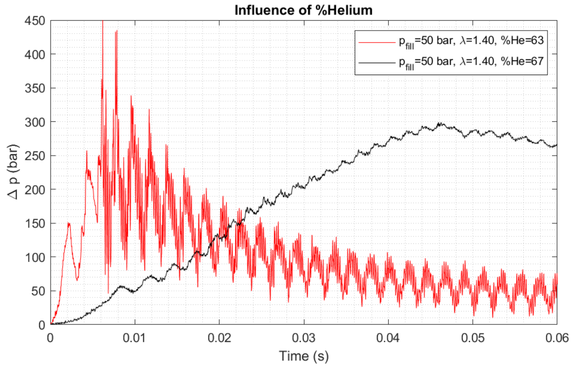

Figure 13: Shots comparison varying %He.

Looking at table 2, the obtained $C.R.$ with the lower helium percentage is higher. This happens because the specific heat of the diluent gas per unit of oxygen concentration increases, and hence the flame propagation decreases as helium is added [7], resulting in a lower pressure rise with increasing dilution. The $\overline{S}$ values have a difference of one order of magnitude, with 259 m/s for the lowest dilution, and 35 m/s for the highest dilution. For the higher diluted mixture, the mass burning rate is around 17 kg/s, and for the other shot, around 131 kg/s. The difference in the order of magnitude is as the one from the flame speed, as it was expected. The average acoustic wave amplitude increases approximately 16 times, from 7 to 111 bar. From equation **??**, we know that the acoustic wave amplitude depends on the heat release. So, as the dilution increases, the total heat release also decreases, and hence, the amplitude of the acoustic waves follows the same behaviour. Besides this, with increasing helium dilution, some flame instabilities that increase the flame area and consequently the heat release, can be suppressed [8].

Table 2: Initial filling parameters and obtained results.

p_{fill} (bar)	λ	% He	$C.R.$	$\overline{S}$ (m/s)	$\overline{\dot{m}_b}$ (kg/s)	$\overline{p_{ac}}$ (bar)
50	1.40	63	9.5	259	131	111
50	1.40	67	7.1	35	17	7

The influence that λ has on the combustion process for high filling pressures ($p_{fill} = 70bar$) can be seen in figure 14. The equivalence ratios of the two shots are $\lambda = 1.27$ and $\lambda = 1.37$, both fuel-lean. By looking at the pressure profiles and table 3, it is clear that for the highest equivalence ratio, the wave amplitude decreases significantly. At high-pressure filling pressures, this behaviour was always observed, and because of that, higher equivalence ratios were used to avoid these high-energy acoustic waves that could transit to detonations. By increasing the amount of O2, the energy release on the flame front decreased. Besides this, O2 is a molecule that can store energy efficiently due to the internal vibrational and rotational modes. But with increasing λ for fuel lean mixtures, the compression ratio, the average flame speed, and the mass burning speed decrease.

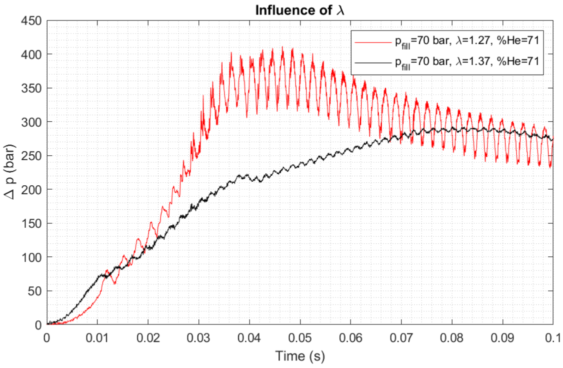

Figure 14: Shots comparison varying λ.

For lower filling pressures ($p_{fill} = 30bar$), λ did not have a strong influence on $\overline{p_{ac}}$, but for mixtures close to stoichiometric conditions ($\lambda \approx 1$), the compression ratio was bigger since the energy release is also maximum.

Table 3: Initial filling parameters and obtained results.

p_{fill} (bar)	λ	% He	$C.R.$	$\overline{S}$ (m/s)	$\overline{\dot{m}_b}$ (kg/s)	$\overline{p_{ac}}$ (bar)
70	1.37	71	5.2	34.41	11.70	7.68
70	1.27	71	7.3	20	13	6

In figure 15, the results of 4 different shots with increasing pressures are presented. The dilution of helium is 71-72% and the equivalence ratio increases with pressure as a consequence of the used methodology. From table 4, the initial filling parameters and the results are given, with λ starting at 1.11 and going to 1.27 for filling pressures of 20 bar to 70 bar. Nevertheless, it can be seen that even with the increased λ, that was proven to decrease the acoustic wave amplitude, $\overline{p_{ac}}$ increases with p_{fill}, as it can be seen from the plot and the values of $\overline{p_{ac}}$ on the table. If the equivalence ratios were all similar, the differences in these values would be more accentuated.

Table 4: Initial filling parameters and obtained results.

p_{fill} (bar)	λ	% He	$C.R.$	$\overline{S}$ (m/s)	$\overline{\dot{m}_b}$ (kg/s)	$\overline{p_{ac}}$ (bar)
20	1.11	72	5.8	44	7	3
30	1.20	71	5.8	44	11	5
50	1.17	72	5.8	32	14	8
70	1.27	71	7.3	34	21	42

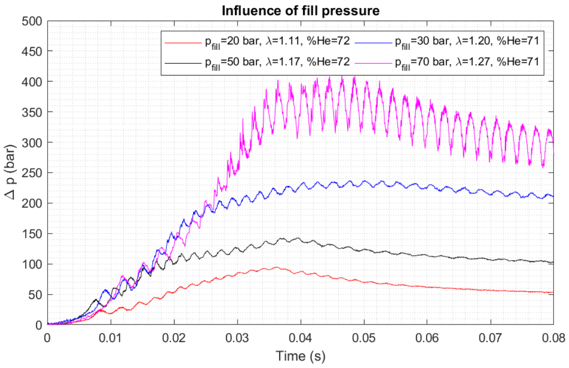

Figure 15: Shots comparison varying filling pressure.

Performance: One of the main requirements for ESTHER combustion driver is high performance, hence, to achieve high post-combustion pressures, up to 600 bar. This goal was achieved during this experimental campaign and the combustion driver performance was proven. In figure 16, the performance range from the highest to one of the lowest-performing shots is given. With the highest performance achieved, it was possible to obtain a post-combustion pressure of 659 bar, slightly higher than the initial requirements. Besides this, it is also possible to operate the driver with pressures below 100 bar if necessary.

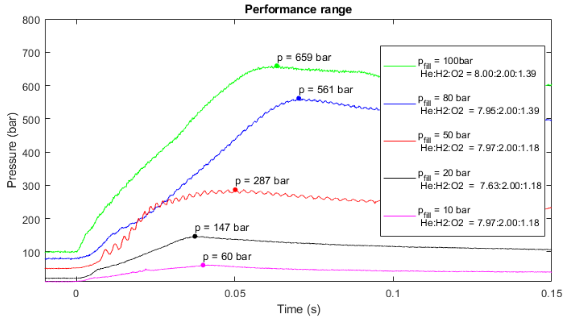

Figure 16: ESTHER combustion driver performance range.

Repeatability: To test the repeatability of the combustion process that took place inside the chamber, some shots were repeated and their signals overlapped to compare the results. In figure 17, an example of this with three shots is given. The initial conditions were $p_{fill} = 10bar$, $\lambda = 0.92{-}0.93$, and $\%He = 57{-}58$. With a helium dilution so low, strong accoustic waves were formed, with amplitudes bigger than the filling pressure at some point. By analysing the overlapping of these three shots, it is possible to obverse that even these very strong accoustic waves are repeatable. Besides the accoustic phenomena, the compression ratio is also very close. The plots when the pressure is decreasing differ, but because the piezoelectric Kistler gauge is not tailored for accurately measuring decreasing pressures.

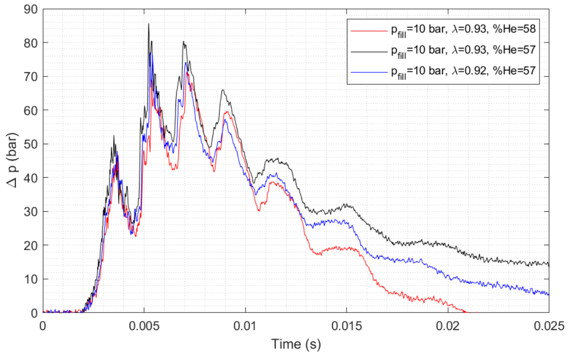

Figure 17: Shots repeatability.

5. Numerical Study

In this section, a numerical study of high-pressure combustion is given. Using the spark code, 2D axisymmetric simulations with He/H2/O2 combustion of a freely expanding flame will be studied. The main focus of this study will be the laminar premixed flame regime and the respective laminar flame speed. Nevertheless, turbulence will also be discussed.

5.1. Governing Equations

In a reacting flow like the case of combustion, the process can be described by the conservation equations from fluid dynamics and chemical composition. These partial differential equations that will model the flow are an extension of classical Navier Stokes equation and are given by equations 5 to 7, where we have the mass conservation equation, followed by the momentum conservation, and the energy conservation equation.

$$\frac{\partial\left(\rho c_i\right)}{\partial t} + \nabla \cdot \left(\rho c_i \mathbf{U}\right) = \nabla \cdot J_i + \dot{\omega}_i \tag{5}$$

$$\frac{\partial(\rho \mathbf{U})}{\partial t} + \nabla \cdot (\rho \mathbf{U} \otimes \mathbf{U}) = \nabla \cdot [\tau] - \nabla p \tag{6}$$

$$\frac{\partial(\rho E)}{\partial t} + \nabla \cdot (\rho E \boldsymbol{U}) = \boldsymbol{\nabla} \cdot (\boldsymbol{U} \cdot [\boldsymbol{\tau}]) - \boldsymbol{\nabla} \cdot \boldsymbol{q} - \boldsymbol{\nabla} \cdot (p \boldsymbol{U}) + \Omega_{\text{tot}}, \tag{7}$$

For equation 5, the diffusion flux $\boldsymbol{J}_i$ of the species i due to mass fraction gradients is given by Fick's Law in equation 8, and $\dot{\omega}_i$ is the production or consumption rate of the species i.

$$\boldsymbol{J}_i \equiv \rho_i \boldsymbol{U}_i = -\rho \mathscr{D}_i \boldsymbol{\nabla} c_i \tag{8}$$

When considering the momentum conservation equation, $[\tau]$ is the viscous stress sensor, and can be modelled with equation 9, where μ is the dynamic viscosity, and $[\mathbf{I}]$ the identity matrix.

$$[\tau] = \mu\left(\nabla \mathbf{U} + (\nabla \mathbf{U})^{\mathrm{T}}\right) - \frac{3}{2}\mu(\nabla \mathbf{U})[\mathbf{I}] \tag{9}$$

For the energy equation, the heat flux vector $\boldsymbol{q}$ is the sum of the conduction heat flux, and the transport of energy by diffusion, given by equation 10.

$$\mathbf{q} = \mathbf{q}_C + \mathbf{q}_D = -k\nabla T + \sum_i J_i h_i \tag{10}$$

To model the transport coefficients μ and κ, the model developed by Wilke is used [9]. In this approximation, it is assumed that all interactions have the same cross-section and inter-species interactions are dismissed. The diffusion coefficient is assumed to be constant for all species and it is given by equation 11, where ρ is the mixture's density, C_p is the mixture total specific heat, and Le is the Lewis number, also assumed to be constant fora all species.

$$\mathscr{D}_i = \mathscr{D} = \frac{Le\kappa}{\rho c_p} \tag{11}$$

5.2. Numerical Set-up

The flow is modelled in 2D axisymmetric, with an implicit time scheme, and an structured and uniform mesh of $10\mu m$. The chemically reacting gas is employed with the kinetic scheme from Burke [10]. The considered domain is a square with a 4 mm side length. Besides the domain limits, the boundary conditions are two symmetry axes, at y=0 mm and x=0 mm, and on the outer region, two subsonic outlets where the static pressure is assigned according to the initial pressure. To ignite the mixture, a Gaussian heat source that initializes the temperature field is employed. The pressure profile on the Gaussian will be constant, and the density profile will obey the perfect gas equation considering the constant field pressure, and temperature distribution. The centre region temperature of the Gaussian was chosen to be slightly below the adiabatic flame temperature of the mixture.

The initial conditions used for the simulations are summarized in table 5, where λ, D, and Le were varied.

Table 5: Initial filling conditions for each simulation.

	Le	p_{fill} (bar)	T (K)	He/H2/O2	λ	%He
Sim. 1	1	5	290	8/2/0.8	0.8	74%
Sim. 2	1	5	290	8/2/1.0	1	73%
Sim. 3	1	5	290	8/2/1.2	1.2	71%
Sim. 4	1	5	290	4/2/0.8	0.8	59%
Sim. 5	1	5	290	4/2/1.0	1	57%
Sim. 6	1	5	290	4/2/1.2	1.2	55%
Sim. 7	1.4	5	290	4/2/1.0	1.0	57%
Sim. 8	0.8	5	290	4/2/1.0	1.0	57%

5.3. Results and Discussion

Flame shape: In figure 18, four time instants of the freely propagating spherical flame of simulation 4 are given. This flame is propagating in a laminar regime, and it can be seen that the flame propagates freely without any disturbances until the fourth time instant. But this behaviour of a perfect spherical flame does not last during the entire simulation time and domain, as it will be shown next.

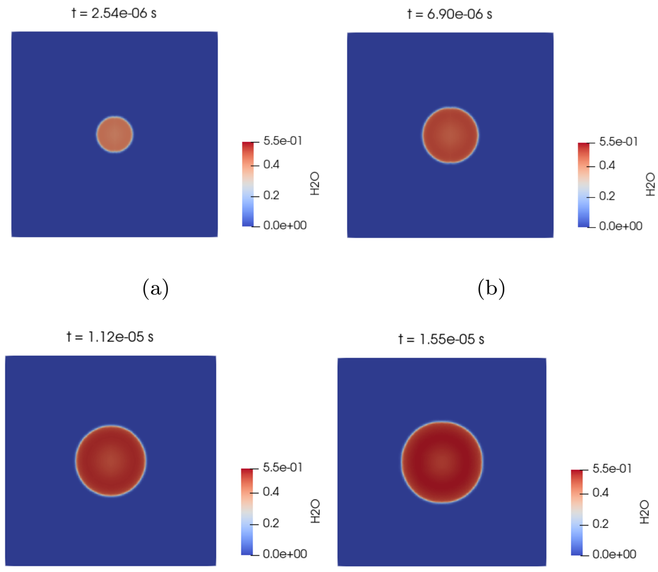

(a) (b)

(c) (d)

Figure 18: H2O mass fraction evolution of simulation 4 (He/H2/O2 ratio of 4:2:0.8).

Flame Radius: The simulations 1 to 3 and 4 to 6 have a constant dilution ratio, $D = 8$ and $D = 4$, respectively, with λ varying from 0.8 to 1.2. In figures 19, the evolution of the flame radius along the simulation time is given for the three different λ mixtures, for $D = 8$ (a) and for $D = 4$ (b). To obtain the flame radius, the considered reference was the temperature iso-line at 1000K.

For both sets of simulations, with different dilutions, the flame radius has a steeper value increase in the first period of time, due to the Gaussian heat source, but the slope tends to a constant value. This slope will be the considered flame velocity, which will be shown next.

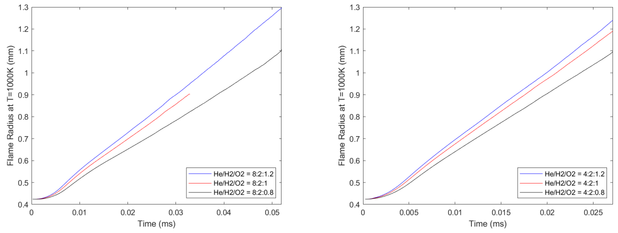

(a) (b)

Figure 19: Flame radius evolution for $D = 8$ (a) and for $D = 4$ (b).

Laminar Flame Speed: To obtain the laminar flame speed, the flow ahead the flame can not be disturbed, and hence, only the values before these instabilities start to occur will be considered for the analysis. In figure 20, the flame propagation speeds for simulations 1 to 6 are given.

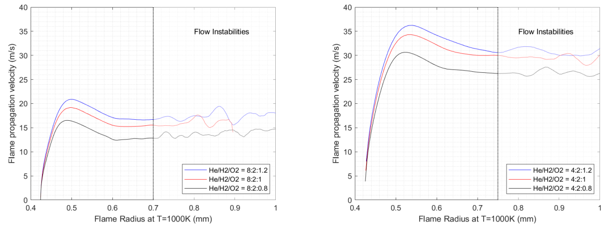

(a) (b)

Figure 20: Flame speed versus flame radius for simulations 1 to 3 (a) and 4 to 6 (b).

Firstly the velocity increases significantly until it reaches the maximum value, and afterward, it decreases and ends converging to a value for most of the simulations. The initial behaviour is still under the influence of the Gaussian used to ignite the gas.

The obtained laminar flame speed values, taken from the stable region of the plot, are the following:

- Sim.1: $S_L \approx 12.6m/s$
- Sim.2: $S_L \approx 15.3m/s$
- Sim.3: $S_L \approx 16.5m/s$
- Sim.4: $S_L \approx 27m/s$
- Sim.5: $S_L \approx 30m/s$
- Sim.6: $S_L \approx 31m/s$

The obtained values are much higher than the experimental unstretched laminar flame speeds obtained by [8]. During the simulations, as the flame front started to propagate outside the Gaussian heat source, a ”temperature shock” developed in front of the flame, increasing the temperature to around 500K, even with different solvers, and in Euler as well. It is assumed that this numerical phenomenon was the main contributor to the discrepancies.

Comparing the results from simulations 2 and 5, for example, the influence that the dilution ratio has on the obtained flame speed is very clear. The S_L value for the lower dilution is almost twice the one from the higher dilution, making these results qualitatively correct.

The flame speed should increase with decreasing λ, but what is observed is the exact opposite behaviour for both sets of simulations. This can be due to the fact that the transport model used assumes that all species have the same diffusion coefficient, and hence, hydrogen diffusion will not play a distinct role in these numerical simulations like what is observed in reality. Besides this, the Lewis number is also assumed to be the same for all species, something that can lead to errors especially with light molecules like H2 [11].

On the right side of the plots, it can be seen that the velocity starts to oscillate considerably. This is due to the fact that in that region, the flow ahead of the flame starts to get turbulent. This can be confirmed by estimating the turbulent Reynolds number from equation **??**, that for $Re_t > 1$ the flow is considered to be turbulent. Assuming a characteristic length scale equal to the flame thickness, the Re_t is given by the ratio between the fluctuation velocity (u') and the unstretched laminar flame speed (S_L^0). Hence, for $u' < S_L^0$, the flame front is considered laminar. It was observed that the flame front started to get more unstable when this condition was satisfied. From this point, the results are not a real representation of a turbulent flame, since turbulence will be mainly a 3D phenomenon. Nevertheless, 2D DNS turbulent flames simulations can also provide a good insight into this phenomena, since for premixed combustion Cant et al. [12] showed that it is more likely to find locally cylindrical (2D) flame sheets, than finding 3D spheroidal flame surfaces.

6. Conclusions

The major goal of this work was to study the high-performance combustion driver of the ESTHER shock tube. This was mainly done in two parts, firstly by studying the influence that the driver has on the performance of ESTHER, followed by the qualification campaign of the combustion driver, where its performance was studied and proven.

It was shown that for the mixtures with helium as the bath gas, the shock tube performance would be almost the double of the performance obtained with N2. Besides the composition, the post-combustion pressure (100 bar to 600 bar) and temperature were varied, where with an increasing values, the main shock speed also increased. For most of the conditions, the test time increases with lower performances.

On the experimental campaign of ESTHER's combustion driver, there were two main goals, proving the performance and operability of the driver, and study high-pressure combustion inside closed vessels. With decreasing He dilution, transitions to detonations were more likely, and the compression ratio, amplitude of the accoustic waves, and the average flame propagation speed increased. With increasing pressure, the onset of detonations got more likely. These accoustic waves were damped with an increasing equivalence ratio, and hence, oxygen richer mixtures. The performance and pressure range of the driver was proven, and repeatability was also achieved.

In the third part of this thesis, a CFD numerical study with high-pressure premixed combustion of He/H2/O2 was given. The laminar flame speeds obtained are much higher than similar experimental conditions, and qualitatively speaking, the results differences when changing the dilution were physical, but not when the equivalence ratio was varied. Although some of the results show that the way the gas was modelled was not suitable, some shortfalls were identified and it still paved the way for future 2D combustion studies using the SPARK code.

References

[1] P. Reynier. Survey of high-enthalpy shock facilities in the perspective of radiation and chemical kinetics investigations. *Progress in Aerospace Sciences*, 85, 2016. DOI: 10.1016/j.paerosci.2016.04.002.

[2] R. A. Alpher and D. R. White. Flow in shock tubes with area change at the diaphragm section. *Journal of Fluid Mechanics*, 3, 1958. DOI: 10.1017/S0022112058000124.

[3] Z. A. Walenta. Optimization of the parameters of a double-diaphragm shock tube. *Archiwm Mechaniki Stosowanej*, 5(19), 1967.

[4] H. Mirels. Test time in low-pressure shock tubes. *Physics of Fluids*, 6, 1963. DOI: 10.1063/1.1706887.

[5] M. Lino da Silv and B. Brotas de Carvalho. High-pressure h2/he/o2 combustion experiments for the design of the esther shock-tube driver. *46th AIAA Thermophysics Conference*, June 2016. DOI: 10.2514/6.2016-4156.

[6] Charles Stark Draper. The physical effects of detonation in a closed cylindrical chamber. Technical report, NASA, 1935.

[7] C. Tang, Z. Huang, C. Jin, J. He, J. Wang, X. Wang, and H. Miao. Explosion characteristics of hydrogen–nitrogen–air mixtures at elevated pressures and temperatures. *International Journal of Hydrogen Energy*, 34, 2009.

[8] S. D. Tse, D. L. Zhu, and C. K. Law. Morphology and burning rates of expanding spherical flames in h2/o2/inert mixtures up to 60 atmospheres. *Proceedings of the Combustion Institute*, 28, 2000. DOI: 10.1016/S0082-0784(00)80581-0.

[9] C. R. Wilke. A viscosity equation for gas mixtures. *The Journal of Chemical Physics*, 18, 1950.

[10] M. Burke, M. Chaos, Y. Ju, F. Dryer, and S. Klippenstein. Comprehensive h2/o2 kinetic model for high-pressure combustion. *International Journal of Chemical Kinetics*, 44, 2012. DOI:10.1002/kin.20603.

[11] Thierry Poinsot and Denis Veynante. *Theoretical and numerical combustion.* RT Edwards, Inc., 2005.

[12] R. S. Cant, C. J. Rutland, and A. Trouvé. Statistics for laminar flamelet modeling. In *Proceedings of the summer program*, page 271. Center for Turbulence Research Stanford, 1990.